Direct 3D Metal Printing: A Trip through New Opportunities and Innovative Alloys

Authors:
Damiano Zito, Dr. Valentina Allodi, Dr. Patrizio Sbornicchia, Stefano Rappo, Luca Fiorese

Abstract:

Direct metal printing is a game changer for creating innovative jewelry. Selective laser melting (SLM™) allows researchers to get creative and think about new materials. This research puts new and different products to the test, exploring fresh horizons for SLM™ utilizing amazing materials for jewelry applications. Additive manufacturing by selective laser melting provides the opportunity to combine materials with very different properties in otherwise impossible ways. What other astonishing new possibilities await as we learn about the surprising properties obtained?

Introduction:

The brief historical journey undertaken so far with selective laser melting (SLM™) allowed managing this manufacturing process with increased safety and versatility, from the early selection experiments of basic parameters and the choice of alloys [1, 2, 3], to the last challenges between the performance of investment casting, and those of selective laser melting in complex decorative elements [4] and, finally, the confrontation with real production needs of jewellers. These promising results have open the possibility of applying selective laser melting to the production of innovative materials of potential interest in jewellery manufacturing.

The current landscape of the gold sector is undoubtedly focused on materials endowed with amazing aesthetic and mechanical characteristics. This study describes some experiments seeking to produce metallic glasses and metal-matrix composites by means of selective laser melting (SLM™). Metallic glasses represent a recent development in precious metal metallurgy [5, 6], and provide extreme hardness alloys with very low processing temperatures. However, producing

these materials using classic casting or investment casting techniques presents limitations when manufacturing thick objects. These limitations arise from high thermal inertia, which prevents the maintenance of the amorphous phase. The selective laser melting technique could effectively circumvent this thermodynamic disadvantage through its rapid cooling, guaranteed by the punctual melting point of the material.

Metallic composites, resulting from the addition of refractory metals in powder form, exhibit new mechanical and chromatic gradients as a function of particular foreign phases, which are suitably introduced into the matrix for the creation of alloys with 18 kt gold content. The selective laser melting technique could represent an alternative technique for producing alloys with refractory metals, elements which are extremely difficult to alloy with gold because of their high melting temperature, notable tendency to slag formation, and high reactivity with crucibles commonly used for melting purposes [7].

Experimental procedure

Precious alloys were pulverised in a gas atomizer and protected by an inert argon atmosphere, producing thus a uniform and dry mass of spherical particles. These conditions are deemed key to obtain good powder flowability when distributing it over the build platform with wipers. Experimental items were printed using the same selective laser melting machine of previous research processes (ReaLizer SLM50), which is equipped with a 100W fibre laser, collimated in a radius of 10 microns.

The shape of powder particles was observed with a scanning electron microscope (Philips, XL 30) and their distribution was determined using a laser granulometer (Malvern, Hydro 2000S). The actual particle distribution was obtained by removing large particles using a stainless steel sieve with a 53-micron square mesh.

Raw materials to synthesise metallic glasses were pre-alloyed in an open casting machine to 700 °C, under an argon-based protective atmosphere, and then poured into a cold iron mould to obtain a homogeneous ingot for atomisation purposes. The alloy composition (1) for the metallic glass laser printing has been chosen among those frequently

cited in the literature, as well as in relevant patents [5]; it contains palladium, copper, silver and silicon alloyed with gold (Table 1). The structural presence of the non-crystalline phase in the alloy was determined by differential thermal analysis (DTA) with alumina crucibles (Seiko Exstar 6300), and by X-ray diffractometry (XRD, Philips PW3710 / 1830 Bragg-Brentano geometry). On the other hand, raw materials to synthesise the precious matrix composite, with the exception of the refractory metal, were alloyed via blasting quenching in water and then pulverized in the atomizer (Table 1). The refractory metal powder was added later and homogenized with the above using a planetary mixer (Glenn Mills, Turbula T2F) to obtain a uniform compound ready for laser melting.

The typical procedure for the construction of a real jewellery item, for example, a glassy-alloy wedding ring, consists particularly in the selection of the best laser parameters, as evidenced in the early works [1, 2, 3, 4].

ALLOY	Au	Ag	Pd	Cu	Si	Nb	Zn	Ti
1	76.26	4.69	1.93	13.5	3.62	0.00	0.00	0.00
2	75.20	0.00	0.00	0.00	0.00	18.5	6.30	0.00
3	75.20	8.40	0.00	0.00	0.00	0.00	0.00	16.4

Table 1 Overall allow compositions (%p) for selective laser melting.

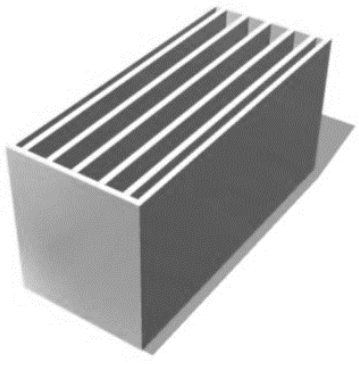

Figure 1 Ideal lamellar sample for vector quality control.

The model used for this primary parameter selection was the classic lamellar solid, constituted by vectors produced by a single laser scan (Figure 1). The lamellar model is a very useful tool to verify the proper melting of the laser line, as well as to detect dangerous porosity and anomalies during vector solidification. In other words, the strength and regularity of individual vectors in these ideal tests constitute the first essential condition to produce dense and reliable jewellery items. Moreover, the printing of individual vectors also allows for the measurement of their width, which is deemed critical for the initial setting of distances between them when building solid pieces.

Progold S.p.A. progold.com +39 (0445) 492600 info@progold.com

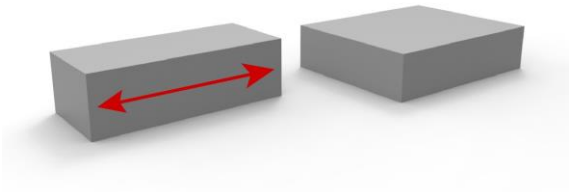

Figure 2 Diagram of solid samples and roughness measurement direction.

Figure 3 Example of samples with bent ends and detachment from supports.

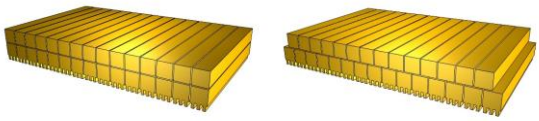

Figure 4 Scan mode with stacked vectors X (left) and placed in the middle X½ (right).

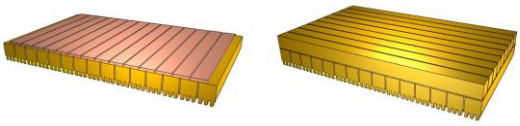

Figura 5 Modalità di scansione con passata centrale XX (sinistra) e rotazione normale delle scansioni XY (right).

On the other hand, the construction of solid (Figure 2) models has been used to optimise the melting strategy, which includes vectors distance, called hatches distance, and laser scanning mode. During the research, two solid model types were chosen depending of the associated working phase. The first solid model is a small rectangular prism (10.0 × 4.5 × 3.0 mm) used in the first research phase, which allows building a large number of pieces on a single platform and, therefore, accelerates the selection of optimal printing parameters.

In addition, the elongated shape of this model allows detecting any shrinkage trend in the alloy, which is usually manifested by a bending of the specimen ends, and its detachment from supports (Figure 3).

After identifying the most promising laser parameter combinations, the second largest solid model (10.0 × 8.0 × 2.5 mm) was used in the second part of the experiment to determine alloy colours. The roughness of printed items was measured using a profilometer (Taylor Hobson®, Form Talysurf INTRA2) equipped with a probe with a 2.0 µm diamond tip. Roughness measurements were performed along the horizontal direction of the two longer faces of the solid models (Figure 2). The hardness was measured on the larger prisms by means of a Vickers hardness tester (Future-Tech, Microhardness Tester FM), with a measurement variability around ±15HV, while the colour was determined using a digital colorimeter (Gretag MacBeth, Color i5).

The number and direction of laser beam traces define the scanning mode along the plane and between construction layers. In this research, we examined five different laser scanning modes. The first scanning mode provides for the simple superposition of laser scans along the vertical direction (Figure 4), indicated by the symbol X, so that the laser beam always scans the same position along all construction layers. The second mode provides for laser scanning in the middle of the vectors of the previous layer, indicated with X½. The third provides a double scan within the same layer, with the second pass in the middle of the vectors of the first pass, indicated with XX (Figure 5). The fourth mode provides for the rotation of the laser scanning

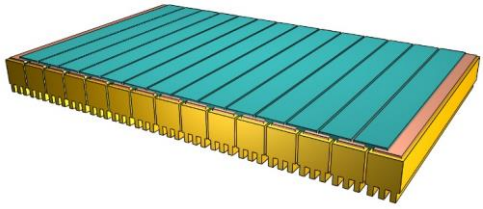

Figure 6 Scan mode with triple XXX laser pass on each construction layer.

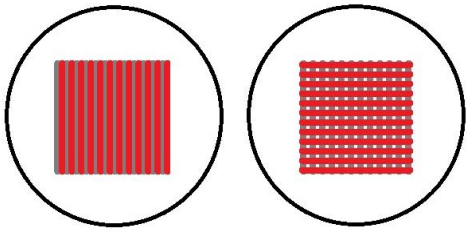

Figure 7 Top view of the scanning placed in the middle XX (left) and of that rotated XY (right).

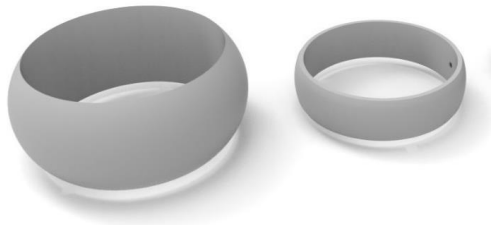

Figure 8 Schematic models of engagement and marriage rings.

perpendicular to the direction of scan of the previous layer, and is indicated by XY (Figure 5), while the fifth and final scanning mode is performed with three consecutive laser scans on the same construction layer, two of them on the same position, and the last between the preceding, which is indicated with the symbol XXX (Figure 6).

The continuous scan rotation may ensure a significant reduction of thermal stress and geometric deformations of the models (Figure 7), while multiple scans generally provide for lower workpiece porosity. Once the series of models planned for the project were produced, the best construction parameter combination for increased piece density and hardness was employed for printing some actual jewellery items.

Selected jewellery includes a hollow ring for the glass alloy, and a massive ring for composite alloys (Figure 8). Figure 9 shows the general flowchart of operations performed in the present research, in which each selection process is followed by a quality control of printed parts to obtain - via exclusion - the most suitable laser parameters for the production of actual jewellery items.

Progold S.p.A. progold.com +39 (0445) 492600 info@progold.com

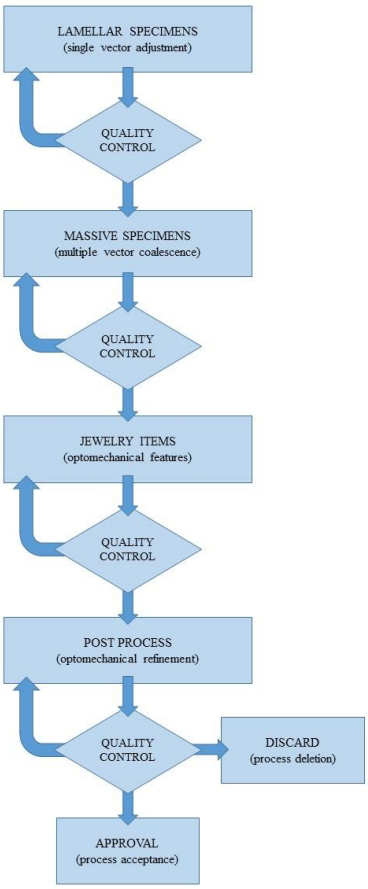

Figure 9 General research flowchart.

Progold S.p.A. progold.com +39 (0445) 492600 info@progold.com

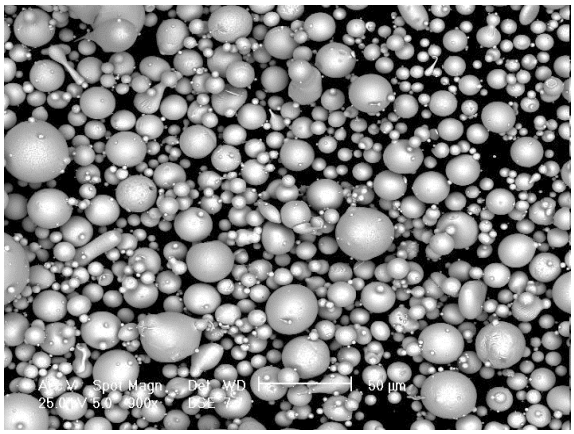

Figure 10 Electron scanning microscopy of the powder of Au76.26Ag4.69Pd1.93Cu13.5Si3.62.

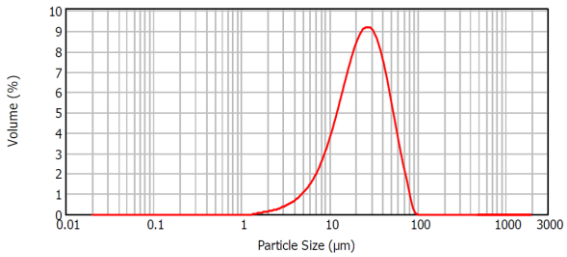

Figure 11 Size distribution of particles in glassy alloy Au76.26Ag4.69Pd1.93Cu13.5Si3.62.

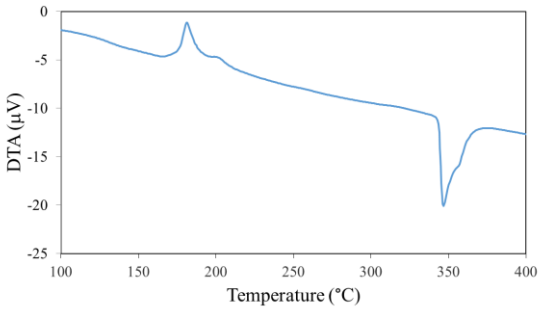

Figure 12 Differential thermal analysis of the glass alloy powder Au76.26Ag4.69Pd1.93Cu13.5Si3.62.

EXPERIMENTAL RESULTS AND DISCUSSION

Amorphous alloy.

The atomization of the metallic glass composition led to the formation of the typical distribution of spherical particles derived from the gaseous atomization of a molten alloy, together with the presence of sporadic, elongated particles (Figures 10, 11). This is probably due to the less than perfect relationship between the atomization temperature (600 °C) and the remarkable viscosity of the molten alloy (1), which arises from the high silicon content. Particles, which represent half of the volume of the powder (D50), have a size of less than 24 µm, while ninety percent of the powder volume consists of particles with a diameter under 51 µm (D90).

The differential thermal analysis (DTA) has confirmed the persistence of metallic glass in the newly atomized powder (Figure 12). The exothermic peak at about 180 °C represents the crystallization process of the amorphous phase, and the endothermic peak around 350 °C indicates the liquidus temperature of the alloy (1). In addition, the alloy glass transition temperature (T_g), detectable by the signal slope change, occurs at around 130 °C, and allows for easy material deformation [8]. The ratio between the area of the first crystallization peak and the melting peak area, which we shall call disorder factor (e_f), is correlated to the lattice disorder and to the amount of the glassy fraction following atomization; the higher its value, the higher the fraction of the amorphous phase. In the newly atomized powder, e_f is approximately equal to 0.63, which, according to literature sources [8], appears to belong to completely amorphous alloys. The measurement uncertainty of the disorder factor is approximately 10%, based on repeated tests on the same sample.

The initial tests were performed with a scan speed of 0.25 m/s in terms of construction of the specimens, while the laser power was ranged from 50 W to 20 W (Figure 13). Pieces offering an

Progold S.p.A. progold.com +39 (0445) 492600 info@progold.com

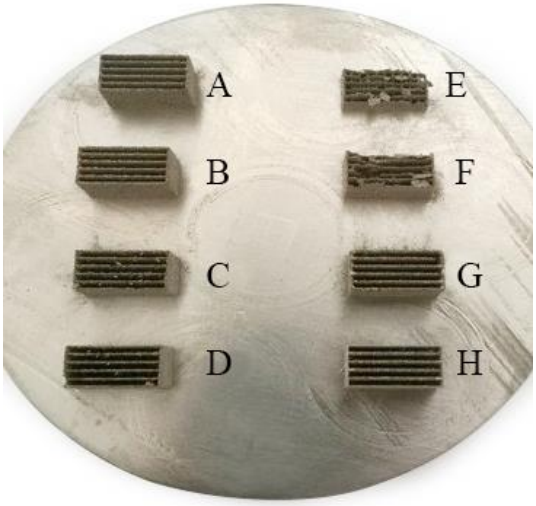

Figure 13 Lamellar vectors as a function of laser power.

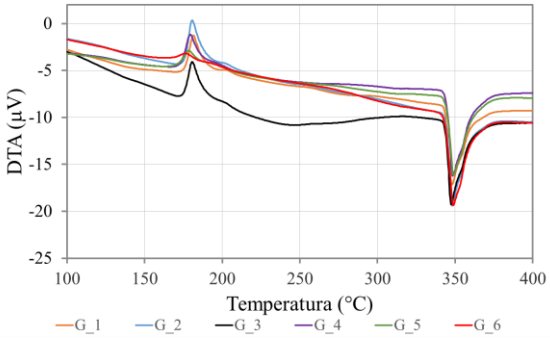

Figure 14 Laser parameters and specimens completion levels as a function of laser power.

acceptable appearance and completeness were built with a laser power between 37.5 W and 50 W. Table 2 shows the laser power and approximate percentage of completion for lamellar pieces obtained from the best platform.

SAMPLE	LASER POWER (W)	COMPLETION (%)
A	37.5	100
B	37.5	100
C	25.0	90
D	25.0	90
E	20.0	20
F	20.0	20
G	50.0	100
H	50.0	100

Table 2 Laser parameters and specimens completion levels as a function of laser power.

In order to maintain a significant fraction of glassy phase in the alloy and a maximum percentage of completion, the scanning speed was gradually increased from 0.25 to 5 m/s. These attempts have been suggested by the lower energy transfer to metallic glass particles, and the consequent reduction in the general overheating, responsible for the increased crystallization phenomenon.

Overall results indicated that, for a laser power of 50 W, lamellar vectors were always completed (100%), while for a power of 37.5 W, pieces were completed only at speeds equal to or less than 0.5 m/s. On the other hand, the disorder factor decreases as the scan speed decreases, as evidenced by differential thermal analysis of the peak crystallization area (Figure 14). For 50 W laser power, the disorder factor reduction and the corresponding scan speeds are shown in Table 3.

Progold S.p.A. progold.com +39 (0445) 492600 info@progold.com

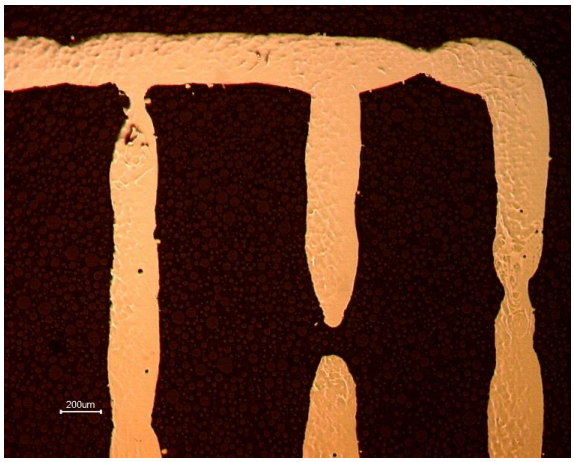

Figura 15 Tipiche anomalie dei vettori con potenza laser di 50 W.

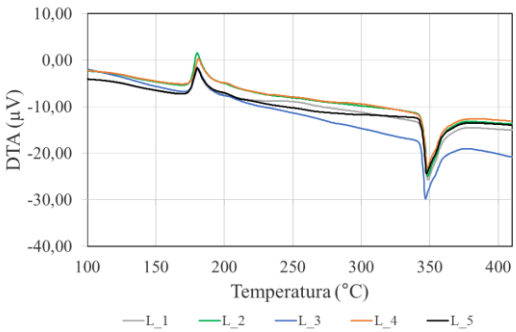

Figure 16 Differential thermal analysis of printed samples with laser power of 62.5 W.

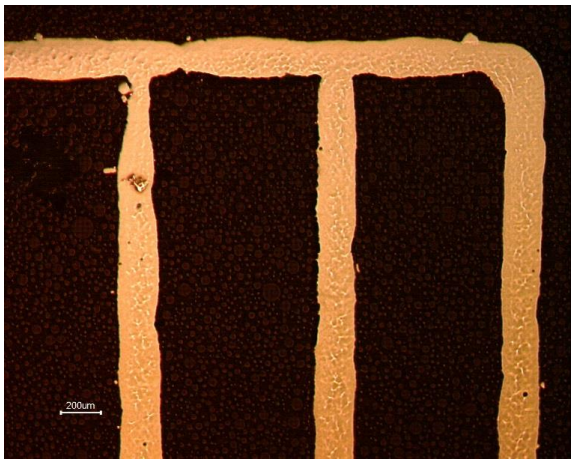

Figure 17 Typical appearance of regular lamellar vectors of sample 3 (Table 4).

SAMPLE	SCAN SPEED (m/s)	e_f
G_1	5	0.52
G_2	2.5	0.57
G_3	1	0.54
G_4	0.5	0.45
G_5	0.33	0.39
G_6	0.25	0.14

Table 3 Laser parameters and specimens completion levels as a function of laser power.

The conservation of a disorder factor for the glass phase close to that of the atomized powder and the maximum geometric completion of lamellar models, however, fail to guarantee the adequate solidity and regularity of printed vectors. The metallographic section revealed the typical imperfections of vectors which were not perfectly solidified, i.e. featuring corrugated profiles and gaps (Figure 15).

The best conditions in order to avoid vector anomalies and maintain an adequate fraction of the glassy phase were encountered by increasing laser power to 62.5 W with a 1 m/s scanning speed, as shown in Table 4. This table also displays samples with identical scanning speed, coming however from various combinations of constituent parameters. The significant persistence of the glassy phase was detected by measuring a strong crystallization signal by differential thermal analysis (Figure 16); the regularity of individual vectors was confirmed by the metallographic section of the corresponding lamellar workpiece (Figure 17).

SAMPLE	LASER POWER (W)	SCAN SPEED (m/s)	e_f
L_1	62.5	5	0.54
L_2	62.5	3.3	0.59
L_3	62.5	1.6	0.47
L_4	62.5	2.5	0.53
L_5	62.5	1.6	0.51

Table 4 Printing parameters and disorder factor for a laser power of 62.5 W.

Progold S.p.A. progold.com +39 (0445) 492600 info@progold.com

Figure 18 Hollow ring after laser printing.

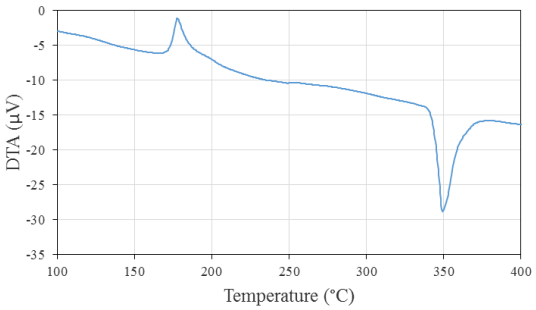

Figure 19 Differential thermal analysis of the ring produced with parameters (B)

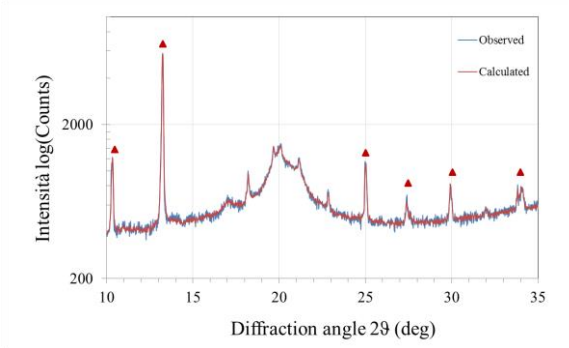

Figure 20 X-ray diffractometry of the ring (B). Internal standard peaks are indicated by a triangle.

Once the proper regularity of individual vectors is achieved, the same construction parameters, i.e. 62.5 W laser power and speed of 1 m/s, were used as initial parameters for the production of solid models (Figure 2) shaped as rectangular prisms (10.0 × 4.5 × 3.0 mm).

The construction tests of solid prisms performed with a scanning mode based on vectors constantly placed in the middle of the previous layers, or in the middle of the same construction layer (X½, XX), have led to better results as regards to overall porosity. The reduction of the hatch distance also tends to reduce material porosity. However, when this distance drops to around 130 µm, brittle fractures begin to appear, bringing the specimen to spontaneous fragmentation, probably because of strong stresses arising from conspicuous material crystallization. Solid samples constructed with the best four parameter combinations (Tables 5 and 6) were also analyzed via DTA and XRD to estimate their glassy fraction. The trend of disorder factor values, determined with DTA technique is in good agreement with the trend of amorphous phase percentage estimated with x-ray diffraction, considering the experimental uncertainty (±10 % DTA, ±5% XRD) and the very different amount of sample analyzed by the two techniques, i.e. 20 mg for differential thermal analysis and 2000 mg for x-rays diffraction, the last corresponding to the whole sample. This difference between two analytical mass can explain the higher crystallinity revealed by thermal analysis for specimen (D) with respect to that measured by x-ray diffraction probably ascribed to the material heterogeneity. Both techniques reveal a good persistence of the amorphous phase in the printed samples, except for the last parameter combination (D), which shows a significant increase in the crystallinity (Table 6).

Progold S.p.A. progold.com +39 (0445) 492600 info@progold.com

Figure 21 Glassy alloy hollow ring after polishing.

Figure 22 Glassy alloy hollow ring after testing in artificial sweat.

ALLOY	SAMPLE	LASER POWER (W)	SCAN SPEED (m/s)	DISTANCE VECTORS (µm)	SCAN
1	A	62.5	1	200	X½
	B	62.5	3.3	200	X½
	C	62.5	3.3	200	XX
	D	62.5	3.3	180	XX

Table 5 Best combinations of laser parameters for the selective laser melting of the glassy alloy.

ALLOY	SAMPLE	L*	a*	b*	Y.I.	R_{tot} (µm)	HARDNESS (HV)	e_f	AMORPHOUS PHASE XRD (% p)
1	A	83.27	1.25	8.45	18.51	69	415	0.48	85.1
	B	81.38	1.04	7.75	17.27	48	401	0.55	83.2
	C	70.04	2.32	10.00	25.70	76	381	0.50	91.2
	D	80.52	0.94	7.85	17.51	39	441	0.21	70.6

Table 6 Optomechanical characteristics of the glassy alloy as a function of laser parameters.

Among the printed jewellery items, i. e. hollow rings similar to an engagement ring (Figure 8), the specimen printed with a laser power of 62.5 W, scanning speed 3.3 m/s, hatch distance of 200 µm, and using a scanning mode X½ (B), revealed the best persistence of the amorphous phase. In this case, in fact, the DTA analysis shows a high calculated disorder factor (ef = 0.54 ± 0.05, Figure 19), confirmed by X-ray diffractometry, which indicates a very high weight percentage of the amorphous phase (92 ± 5%, Figure 20).

The aesthetic appearance of this ring is characterized by a good geometrical coherence with respect to the digital model, but there is a significant overall roughness (Figure 18) and porosity was still significant, albeit less than that observed with other parameters. Unfortunately, the most serious problem when manufacturing this glassy alloy lies in the finishing process and colour stability.

In fact, it was generally observed that the grinding and polishing can easily produce localised specimen deformation, because of the overheating under the process brushes, and the low softening point of the material. In this case, it might be better to rely on finish systems which can keep the specimen at a relatively low temperature, such as tumbling and electropolishing.

The glassy alloy was also examined in terms of

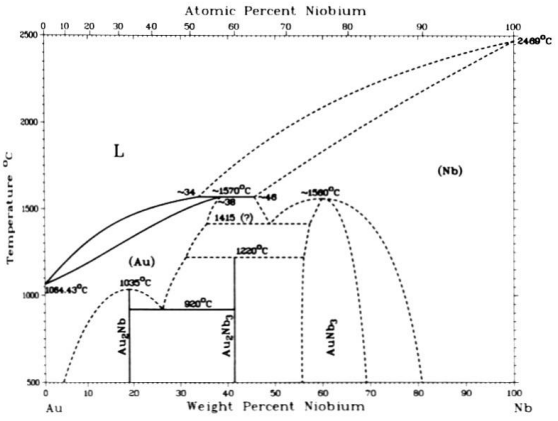

Figure 23 Binary phase diagram for the niobium-gold system.

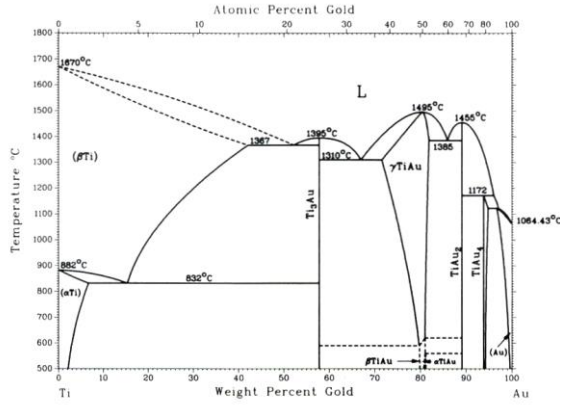

Figure 24 Binary phase diagram for the gold-titanium system.

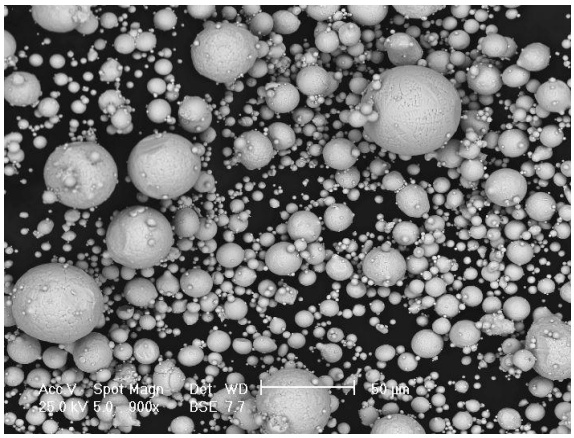

Figure 25 Scanning electron microscopy of the zinc-gold matrix

colour stability, as this kind of material presents a very low resistance to oxidation. The oxidation resistance test was conducted for seven days using artificial sweat consisting of sodium chloride, urea, and lactic acid according to standard procedure (UNI EN 1811: 2015), in order to to assess any optical alteration. The colour difference between the freshly polished ring and the ring exposed to synthetic sweat was very significant (Figures 21 and 22).

Composite alloys

Selective laser melting was subsequently used for the synthesis of gold alloys with refractory metals. This metal family has a high melting point and high wear resistance, and the current extended definition includes fourteen elements (Ti, V, Cr, Zr, Nb, Mo, Ru, Rh, Hf, Ta, W, Re, Os, Ir), each of which presents serious application difficulties in jewellery due to their poor solubility in gold and high reactivity with oxygen, nitrogen and the melting crucible. Niobium and titanium, for example, are generally employed as hardening and reinforcing additives in structural alloys, such as stainless steel and aerospace alloys. Their solubility in precious metal matrices is relatively restricted in normal conditions; however, these metals have a remarkable whitening and hardening power, an aspect which makes them very desirable in jewellery (Figures 23, 24).

To overcome these problems and preserve the advantageous performance of both elements, we conducted a series of selective laser meltings for each refractory metal on mixtures of two different powder types. The first powder type is obtained by alloying gold via atomization with an auxiliary metal (Ag, Zn), and constitutes the precious matrix of the final mixture, while the second type is constituted by the pure refractory element. Both powder types are then suitably mixed according to a specific ratio using a planetary mixer to obtain the final alloy compositions (Table 1).

The auxiliary metal acts as a limit to the addition of refractory metal, which could hinder the melting or form critical amounts of brittle intermetallic, as well as a way to adjust the fineness of printed

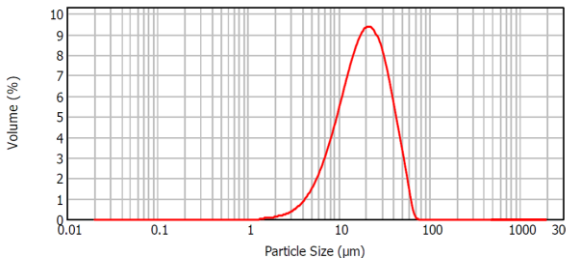

Figure 26 Particle size distribution of the zinc-gold matrix.

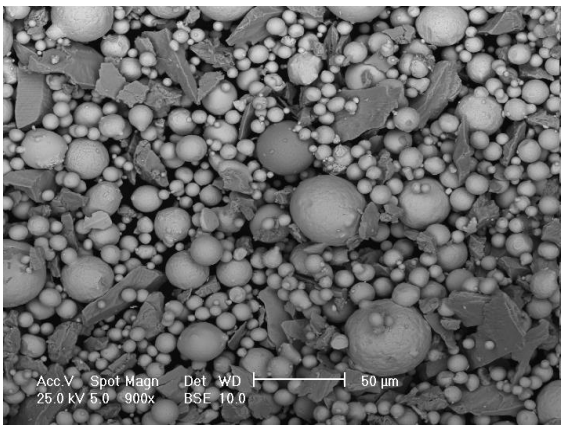

Figure 27 Scanning electron microscopy of the powder mixture for the alloy (2).

material; the precious matrix serves to uniformly disperse the refractory metal, while allowing the most quantitative solubilisation possible.

The first composite alloy (2) analysed is based on a precious metals matrix formed by 92.5%p gold and 7.5%p zinc (Figure 25), to which niobium powder was then added up to a final content of 18.5%p. The zinc alloy used by way of auxiliary metal may affect the production quality when using the selective laser melting technique. On the other hand, due to its low melting (420 °C) and boiling (907 °C) point, it may provide unexpected advantages, once the laser power has been calibrated. The composition of this alloy did not cause particular atomization problems; in fact, the powder morphology (Figure 25) and the dimensional particle distribution (Figure 26) obtained correspond to the standard process characteristics, with a D50 equal to 19.3 µm and D90 to 40.3 µm. The morphology of the powder mixture in the precious matrix shows good homogenization of the refractory metal, and acceptable dimensional comparability, although the niobium particles used for this preliminary research were polygonal rather than spherical (Figure 27). In general, it is known that spherical shaped particles are better for selective laser melting, however, for this introductory research, we used polygonal shaped niobium particles because of their easier reperibility on the market. In any case, the presence of non-spherical particles had no impact on the flowability of the mixture, both under the Carney (ASTM B417-89) or Hall (ASTM B213-03) test, with respective values of 2.3 and 8.8 s for the drop of a 50g powder mass. Further analyses with spherical niobium particles are being conducted to perform an impact assessment of the refractory element morphology on printing results.
Similarly to the glassy alloy, the best combination of print parameters was chosen from lamellar and solid models. The four laser parameter combinations and the properties of related samples are listed in Tables 7 and 8.

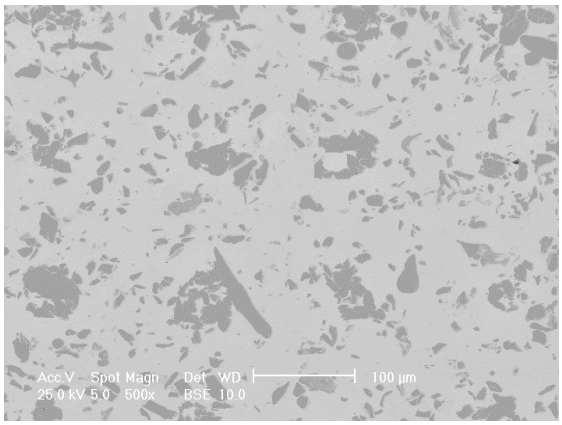

Figure 28 Scanning electron microscopy of the alloy (2) after laser printing (B).

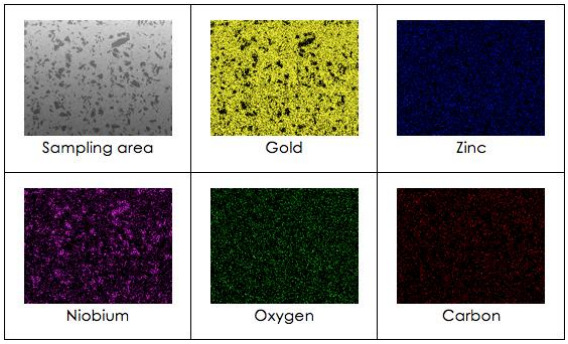

Figure 29 Element map for the alloy (2) after laser printing.

ALLOY	SAMPLE	LASER POWER (W)	SCAN SPEED (m/s)	DISTANCE VECTORS (µm)	SCAN
2	A	37.50	0.25	130	XY
	B	37.50	0.25	150	XY
	C	37.50	0.33	130	XY
	D	43.75	0.33	150	XY

Table 7 Best parameter combinations for selective laser melting of Au-Zn-Nb 750 ‰ (2)

ALLOY	SAMPLE	L*	a*	b*	Y.I.	R_{tot} (µm)	HARNESS (HV)
2	A	77.92	1.39	11.15	24.94	62	266
	B	80.43	1.73	11.69	24.38	63	292
	C	72.62	1.64	11.85	27.99	58	272
	D	76.32	1.31	10.04	23.08	59	274

Table 8 Optomechanical characteristics as a function of laser parameters for the alloy (2).

In the case of composite materials with niobium, the general characteristics of printed objects evidence a precious matrix consisting of a gold-zinc solid solution, which embeds the niobium particles.

This polygonal niobium particles (Figure 28) are most likely due to their incomplete solubilisation in the newly printed samples, probably because of the intrinsic rapidity of the selective laser melting process, which does not provide the adequate dissolution time for the entire refractory mass of niobium. On the other hand, the atmosphere of relatively pure argon (<0.1% O2) and the speed of the local melting process help prevent the oxidation of niobium.

The element map showed the distribution of individual metals in the alloy (Figure 29), revealing that, besides particles of almost pure niobium, also the precious metal matrix contained niobium, thus confirming at least the partial solubilisation of the refractory metal.

These niobium particles (10 - 50 µm) constitute a structural reinforcement for the zinc-gold matrix,

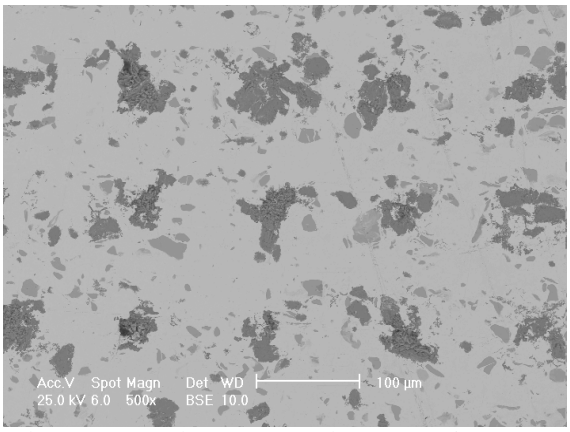

Figure 30 Scanning electron microscopy of the alloy (2) after solubilisation at 680 °C for 30 minutes (N_2/ H_2).

even if they hinder the achievement of a true solution in the solid state. The precious metal matrix wets and adheres to the niobium particles in solid state without solution of continuity. Upon visual inspection, the presence of these uniformly distributed niobium particles may alter the brightness of the final jewellery item. The relative disadvantage of the optical noise due to the presence of niobium particles could be reduced by furtherly promoting atomic diffusion of niobium in the precious matrix.

Printed items are checked for gold content, with particular focus on accuracy and homogeneity. These analyses, conducted with X-ray fluorescence techniques (Bruker Tiger 8, Thermo Scientific Niton XL2 800P) and cupellation (UNI EN ISO 11426: 2000), have revealed a considerable lack of uniformity in gold content, which ranges between 70% and 78%. This wide variability could arise from the use of non-spherical niobium particles, which may have somehow favoured a non-homogeneous distribution of the mixture elements on the printing table. In addition, the different width of the particle size distribution of the powders used may have played an important role in this result, given the tendency of smaller fraction particles, which are present only in the precious matrix, to settle down during the printing process. To counter this issue, in addition to the planned tests with spherical niobium particles, subsequent studies will be oriented towards the use of powders with a particle size purged of the smallest fraction and of equal size distribution between precious matrix and refractory metal.

In order to improve the diffusion of non- dissolved niobium particles, solubilisation treatmend were carried out. The first attempt to solubilize niobium particles has been performed from a temperature of 680 °C (Figure 30); this treatment, however, failed to achieve a complete diffusion of the refractory metal.

Solubilisations at higher temperatures (750 °C, 800 °C) have instead resulted in significant reductions of pure niobium particles initially included in as printed articles (Figure 31, 32), probably due to the absorption of refractory metal by the precious matrix. In addition, at a

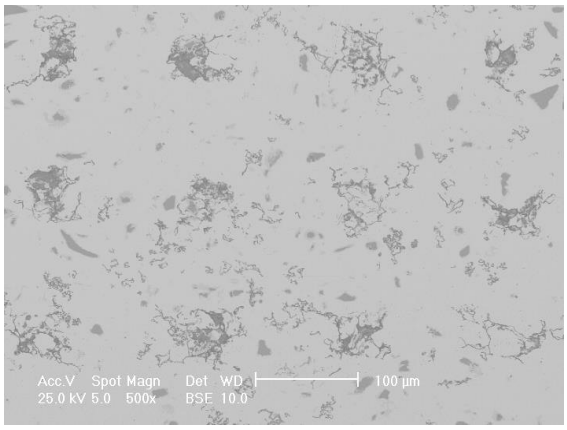

Figure 31 Electron microscopy of the alloy (2) after solubilisation at 750 °C for 30 minutes (Ar).

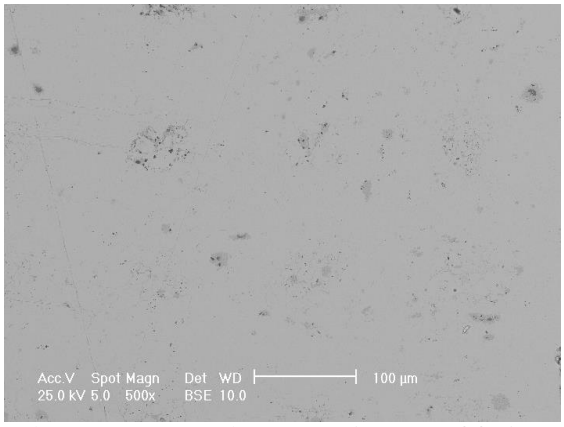

Figure 32 Electron microscopy of the alloy (2) after solubilisation at 800 °C for 30 minutes (Ar).

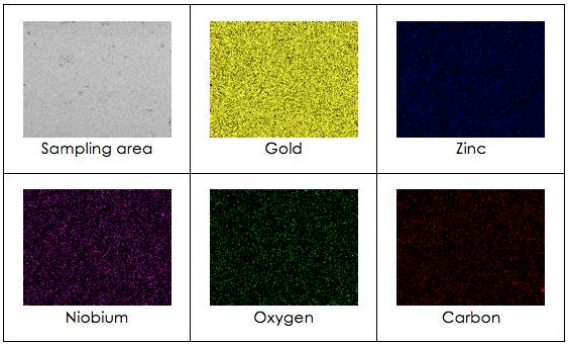

Figure 33 Map of alloy elements (2) after solubilisation at 800 °C (Ar).

temperature of 750 °C, the internal porosity of the material increased, due to the residual cavities left by the disappearance of pure niobium particles. Conversely, at a temperature of 800 °C, this tendency appears substantially lower, probably because of the higher material densification. Porosity is in turn responsible for the hardness reduction observed in solubilized samples at 750 °C, relative to values obtained with the solubilisation treatment at a lower temperature (Table 8). In the case of the sample treated at 750 °C in N_2/ H_2, we also observed a significant variation in the yellow index, which might be due to a partial reaction of niobium with the nitrogen present in the eviroment. In addition, given the high percentage of niobium, even small amounts of oxygen present during the solubilisation process can lead to the formation of large quantities of niobium oxide, which are visible in the electron microscope as dark masses already for the 680 °C treatment (Figure 30). While these particles can help increase the sample hardness, they prove problematic when polishing specimens afterwards. Treatments at 750 °C and 800 °C in a protected argon atmosphere have therefore been performed in a closed system, with repeated washings of the inert gas, producing the best results under this point of view, with a much lower oxide incidence (Figure 31, 32). The remarkable solubilisation of niobium at 750 °C provides a yellow index equal to 17.08, corresponding to a premium white colour, while increasing the specimens hardness to 319 HV (Table 9). In the case of treatment at 800 °C, solubilisation was almost complete, as confirmed by the map (Figure 33); nevertheless, the hardness and yellow index were slightly worse, probably due to a reduction in the amount of intermetallic compounds in the material resulting from the higher temperature.

Figure 34 Solid ring printed with alloy (2) and laser power of 37.5 W (A).

Figure 35 Newly printed, alloy solid ring (2) after polishing

Figure 36 Alloy solid ring (2) after solubilisation and polishing.

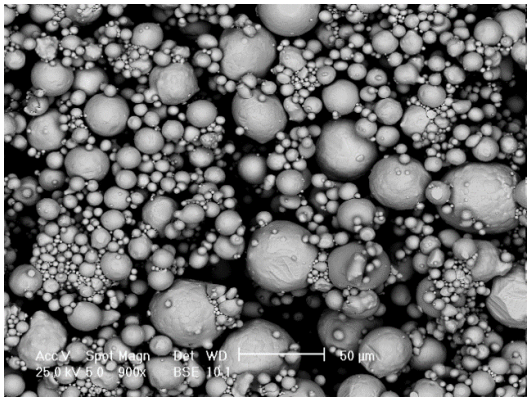

Figure 37 Scanning electron microscopy of the silver-gold matrix

TEMPERATURE (°C)	GAS	L*	a*	b*	Y.I. (D1925)	HARDNESS (HV)
after printing (A)	Ar	77.92	1.39	11.15	24.94	266
after printing (B)	Ar	80.43	1.73	11.69	24.38	292
680°C 30 min (A)	N_2/H_2	77.19	0.86	6.04	14.29	366
750°C 30 min (A)	N_2/H_2	78.40	1.49	13.43	29.25	210
750°C 30 min (B)	Ar	75.31	1.23	7.60	17.08	319
800°C 30 min (B)	Ar	83.88	0..8	8.83	18.55	278

Table 9 Optomechanical characteristics (2) after solubilisation at various temperatures.

The following parameter combination (A) was chosen for the solid ring construction: laser power 37.5 W, scanning speed 0.25 m/s, and hatch distance 130 microns. Once polished, rings appear white (Figures 34, 35). The polishing of the newly-printed wedding ring still shows a certain degree of satin-finish because of the heterogeneous phases rich in niobium, even if they appear very uniform. We introduced a heat solubilisation treatment to reduce surface satin-finish on this type of rings, which has however raised their brightness (Figure 36).

The last alloy with refractory metals used in selective laser melting contains titanium and silver as auxiliary elements, which are meant to replace zinc. The atomized matrix is constituted by 90%p of gold and 10%p of silver, which was added to the titanium powder so that the final content of this refractory element equals 16.4%p and that of gold 750‰ of the alloy (3).

The morphology (Figure 37) and particle size distribution of the binary gold-silver pre-alloy powder (Figure 38) are consistent with the first matrix (Au-Zn), although the trend favours slightly larger sizes (30 µm). The appearance of the mixture of precious matrix powder and titanium is more uniform compared to previous cases, given that refractory metal particles have a spherical shape of a similar size compared to the matrix (Figure 39).

Unlike niobium (Tm = 2477 °C, ρ = 152 nΩ·m), titanium tends to solubilize much better in selective laser melting, probably due to its much lower melting temperature, and three-times higher

Progold S.p.A. progold.com +39 (0445) 492600 info@progold.com

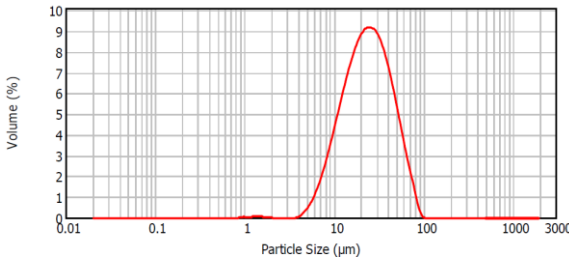

Figure 38 Particle size distribution of the gold-silver matrix.

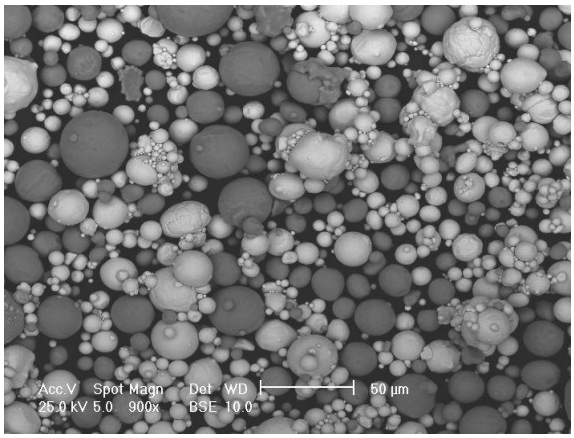

Figure 395 Scanning electron microscopy of the powder mixture for the alloy (3).

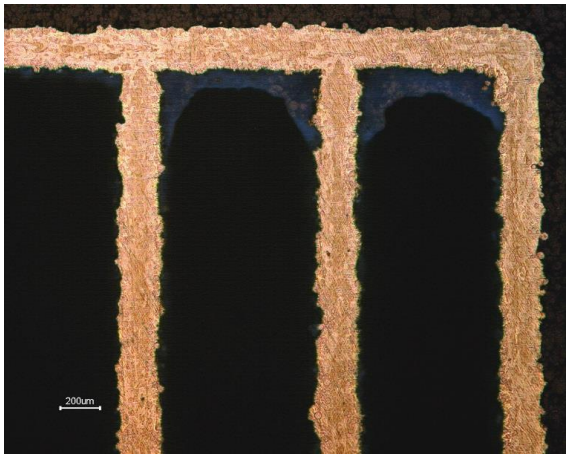

Figure 6 Scanning electron microscopy of the powder mixture for the alloy (3).

electrical resistivity (Tm = 1668 °C, ρ = 420 nΩ· M), which entails a more effective absorption of laser radiation. The item microstructure, therefore, presents a smaller presence of inclusions of titanium particles already in its as-printed raw state. In this case, the printed material is much closer to a real solid state solution than to a metal matrix composite, since the amount of reinforcing particles of pure titanium can be really small, depending on the combination of laser parameters applied.

The preliminary melting of vectors and solid prisms showed a fairly unique phenomenon for gold powders with high titanium contents. The laser irradiation at the point of contact with the powder produces a significant scatter of molten lapilli, which dirties other growth regions in the specimen. Notwithstanding the above, the best among the lamellar models used for quality control of the linear melting of individual vectors show good continuity of material cords (Figure 40), although the vector profile appears quite ripped. Individual vectors appear to consist of irregular portions of variable composition materials, due to the partial homogenization of titanium with the precious matrix.

In the case of solid models, the lapilli phenomenon requires capping the laser power at 50 W, or using a multiline scanning mode (XXX), which begins with a first scan at very low power (20 W), and two high-power ones afterwards. As with previous cases, a group of four laser combinations was chosen for the titanium alloy (3), with a view to obtain the best conditions for metal solubilisation and microstructural integrity. The hatch distance was held constant at 150 µm, similarly to the scanning speed, which, however, arises from different combinations of exposure time and distance of the laser pulses (Table 10 and 11). Scan modes used were XX and XXX.

Progold S.p.A. progold.com +39 (0445) 492600 info@progold.com

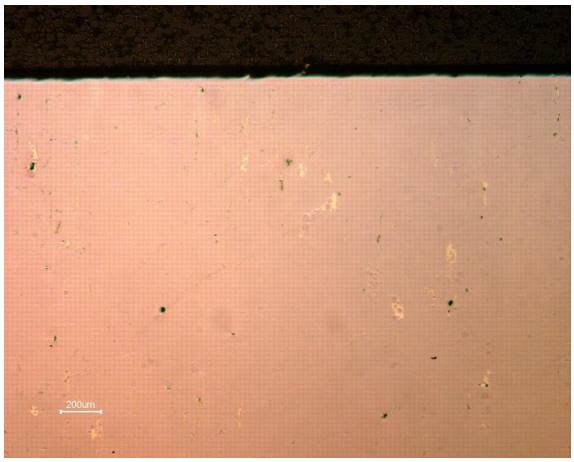

Figure 41 Example of a metallographic section of Au-Ag-Ti alloy (B) solid prisms.

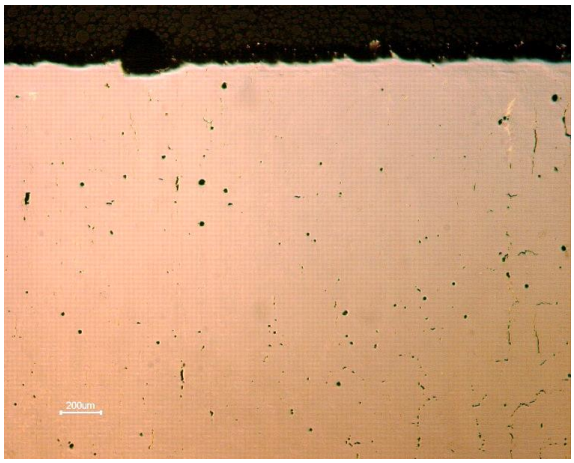

Figure 42 Metallographic section of the solid prism (D) with obvious formation of cracks.

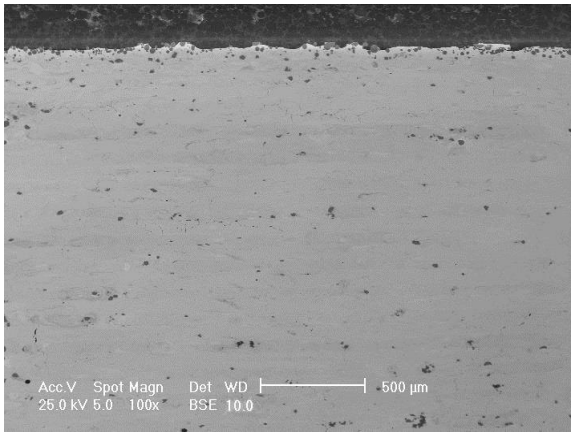

Figure 43 Electron roscopy of the solid prism (A).

ALLOY	SAMPLE	LASER POWER (W)	SCAN SPEED (m/s)	DISTANCE VECTORS (µm)	SCAN
3	A	50	0.25	150	XX
	B	20 - 75 - 50	0.25	150	XXX
	C	20 – 62.5 - 45	0.25	150	XXX
	D	50	0.25	150	XX

Table 10 Best parameter combinations for selective laser melting of Au-Ti-Ag 750 ‰ (3).

ALLOY	SAMPLE	L*	a*	b*	Y.I.	R_{tot} (µm)	HARDNESS (HV)
3	A	78.85	0.67	5.98	13.72	53	274
	B	78.80	0.55	5.50	13.22	54	288
	C	78.83	0.74	5.59	12.60	61	293
	D	78.78	0.70	6.50	14.83	56	279

Table 11 Optomechanical characteristics as a function of laser parameters for the alloy (3).

The hardness measured on these samples can reach values close to 300 HV and, therefore, be significantly higher than that of a classic white gold alloy 750 ‰ with a similar content of nickel equal to 12%p (240 HV), when as-casted (Table 11). In addition, the yellow index can drop to exceptionally low values (YI D1925 = 12.60), lower than those of pure palladium (YI D1925 = 13.63).

In general, the metallographic analysis of solid prisms constructed with the best parameters (Table 10) revealed a good side connection of vectors, with low porosity predominantly found on vector edges, and sparse areas showing light and dark streaks following the laser scan pattern, which indicates local inhomogeneity in the titanium content (Figure 41). The average porosity detected from the analysis of digital metallographic sections was comparable for all samples, with a mean value of 0.22 ± 0.04% in the area analysed. Sample (D) (Figure 42) also showed a significant number of cracks, mainly in-between vectors, although some running perpendicular to them. This arrangement suggests that the formation of cracks arises from thermal stresses developed during printing, rather

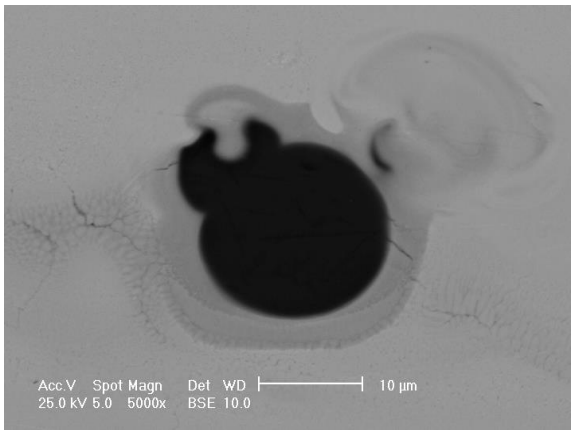

Figure 7 Electron microscopy of a titanium particle (C).

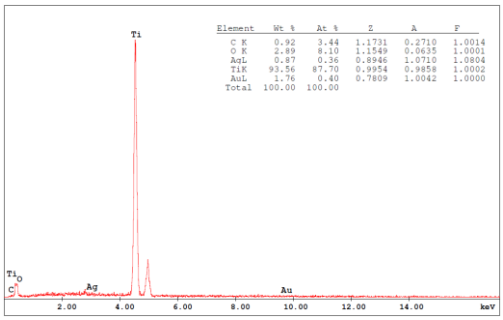

Figure 8 Microanalysis (EDX) of a titanium particle included in the metallic mass (A).

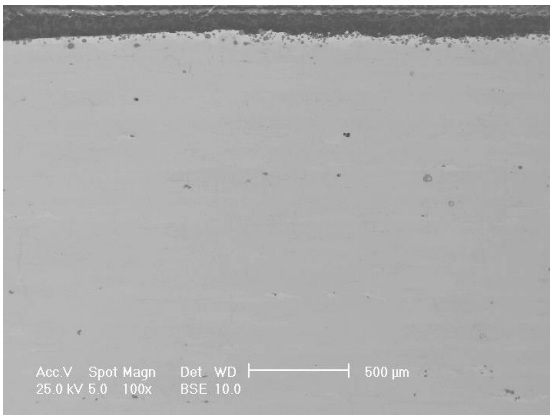

Figure 9 Typical electron microscopy of prisms B, C and D.

than from a partial side connection of vectors resulting from imperfect printing parameters. This may indicate a lack of intrinsic ductility of the material due to its composition; in fact, although the titanium content was chosen so as to bring the alloy system closer to the stability region of the γAu-Ti phase (Figure 24), which offers a certain ductility [9], the presence of silver metal as auxiliary element may be responsible for the reduction of the alloy plasticity for the formation of intermetallic compounds ($AgTi_2$) with titanium.

The same prisms observed under the electron microscope confirmed the findings of metallographic analysis, highlighting the presence of titanium particles trapped in the matrix, in particular in sample (A) (Figure 43). The magnification of one of these particles is presented in Figure 44. The EDX microanalysis confirms a composition consisting of almost pure titanium in the centre of the particle (Figure 45), and a transition halo with intermediate composition between particle and matrix. For samples printed with parameters B, C and D, the presence of titanium particles is much reduced (Figure 46). Moreover, all electronic images display a surface layer of a few tens of micrometres holding numerous unresolved titanium particles and simply incorporated by the precious matrix.

The confirmation of the almost complete solubilisation of titanium can be also obtained from the element map in a polished section of a solid prism (Figure 47). Titanium appears quite uniformly dispersed, although an unchanged particle and a porosity are still visible. The oxygen present does not appear concentrated in refractory particles, but evenly distributed inside the material. This means that printing conditions were characterized by an oxygen content which was sufficiently low to avoid titanium oxidation.

Thanks to the almost complete solubilization of the titanium following the simple printing, the yellow index for the alloy (3) can drop to value lower than those observed for the niobium alloy (2) before solubilisation.

The metallographic etching of a horizontal section of a solid prism reveals the presence of a fairly homogeneous, long range microstructure,

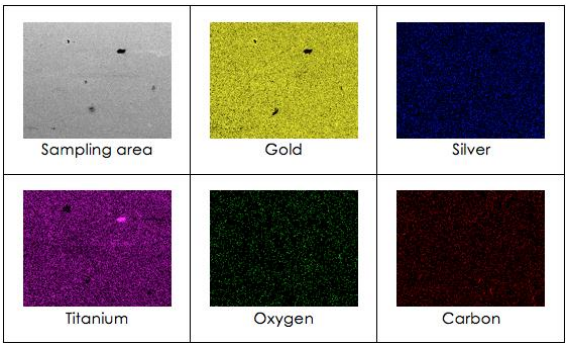

Figure 10 Element map for the alloy (3) after printing.

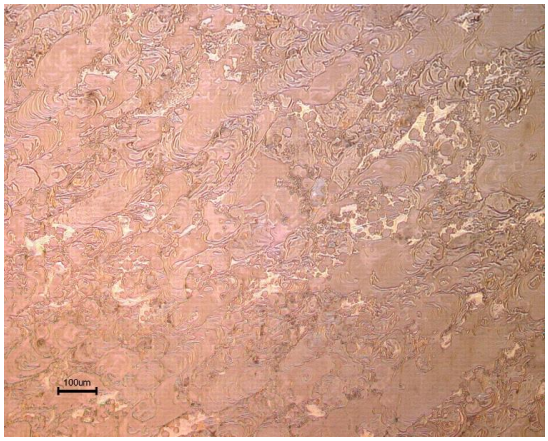

Figure 11 Metallographic section after chemical attack (100X) of the solid sample (A)

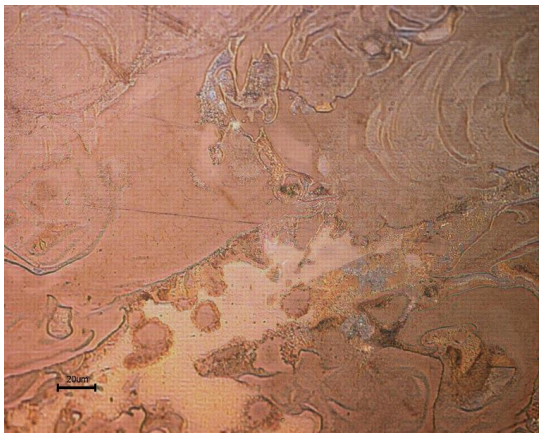

Figure 49 Metallographic section after chemical attack (500X) of the solid sample (A)

whereas phase concentration areas are evident at local level (Figure 48). The metallographic examination also evidences the traces of the laser scans, and a certain degree of vector intermixture, which favours specimen consolidation. The grain structure is appreciable only in a few small areas under high magnification (500X, Figure 48 and 49), showing a crystal size of around 10 µm, given that the solidification kinetics and the small melted area prevent the growth of grains visible with the optical metallographic microscope.

Similarl with niobium, the gold content of titanium alloy, measured with the same analytical techniques, showed a very similar overall variation range, that is to say between 700‰ and 780‰. This strong similarity suggests that the gold content heterogeneity is not solely attributable to the particle shape, that is irregular for niobium and spherical for titanium, but rather to the possible sedimentation of the precious particles on the working table, which can take place in both situations.

Although in the case of titanium the starting microstructure is much more homogeneous than that of niobium, some thermal solubilisation treatments were however operated on solid prisms to reach the complete material homogenization. Unfortunately, results obtained were not satisfactory. The hardness reduction and the yellow index increase relative to the as-printed condition (Table 12) indicate a behaviour contrary to that expected for niobium.

After a solubilisation treatment at 900 °C for 30 minutes, titanium show a substantial tendency to remain confined and unchanged within the initial particles, as shown by the electron microscopies made at the same previous positions (Figures 50 and 51). On the other hand, as a result of this heat treatment, it is already appreciable a discrete increase in cracks and a slight rise of titanium diffusion towards the matrix, evidenced by the thickening of the dark grey crown around the same pure titanium particle (Figures 44 and 54).

Progold S.p.A. progold.com +39 (0445) 492600 info@progold.com

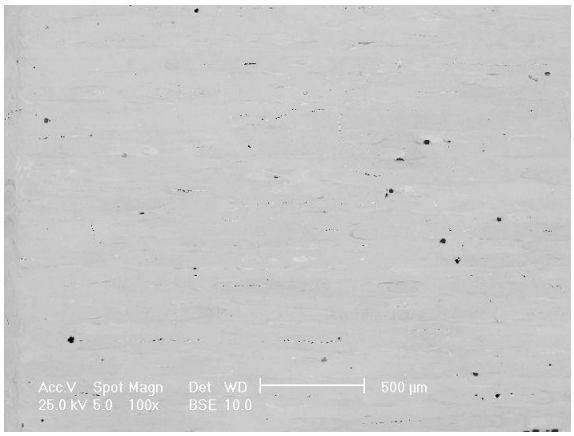

Figure 50 Scanning electron microscopy (100X) of alloy (3) after printing (C).

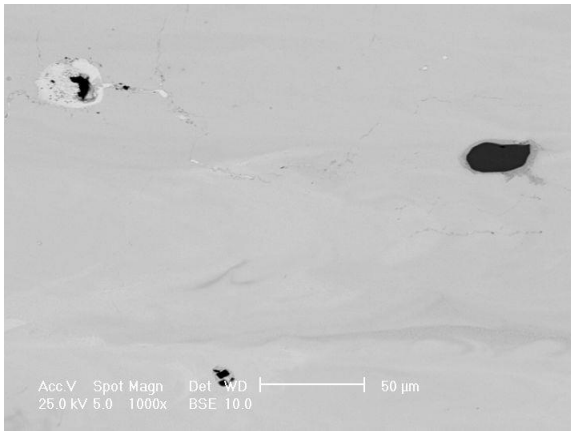

Figure 12 Scanning electron microscopy (1000X) of alloy (3) after printing (C).

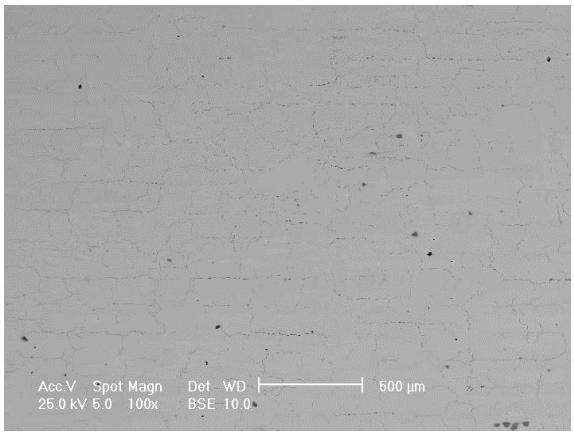

Figure 52 Scanning electron microscopy (100X) of alloy (3) after solubilisation at 900 °C.

TEMPERATURE (°C)	GAS	L*	a*	b*	Y.I. (D1925)	HARDNESS (HV)
After printing (C)	Ar	78.83	0.74	5.59	1.60	293
900°C 30 min	Ar	79.20	0.67	6.43	14.37	271
1100°C 30 min	Ar	78.66	1.07	6.49	15.02	274

Table 12 Optomecanichal characteristics (5) after solubilisation at various temperatures.

The formation of cracks is another factor that tends to increase with the solubilization temperature. In fact, treatment at 1100 °C produced a significant increase in cracks and titanium diffusion, which, however, tends to react with the silver around its original particles (Figures 55 and 56).

Dark grey halos (Figure 56) around cracks are in fact composed of relatively high percentage of silver, compared to the nominal value of the alloy (3). Solubilisation at a higher temperature can cause the almost complete absorption of titanium particles by the matrix; in fact, dark speckles visible in electronic microscopy in Figure 55 belong only to the material porosity.

This silver and titanium concentration in the vicinity of the cracks can be also confirmed by the elements map after solubilisation at 1100 ° C (Figure 58). The atomic ratio between the elements probably indicate the formation of the intermetallic Ti_2Ag, which may be the less ductile material of the element, and hence primarily responsible for the crack appearance.

According to metallographic results, the control ring has been printed with a multiline scanning mode (XXX) to reduce the formation of porosity and increase titanium solubilization (B). The complete resorption of the refractory metal particles by the precious matrix is preferable, given that, during the finish phase, the surface shows a glossier and shinier appearance. although it is possible to consider it a natural defect, as the definition of composite material includes the presence of phases extraneous to the matrix.

The yellow colour of the newly printed ring (Figure 59) can be explained by the presence of a surface layer - in the tens of micrometres range - rich in undissolved titanium particles, and simply

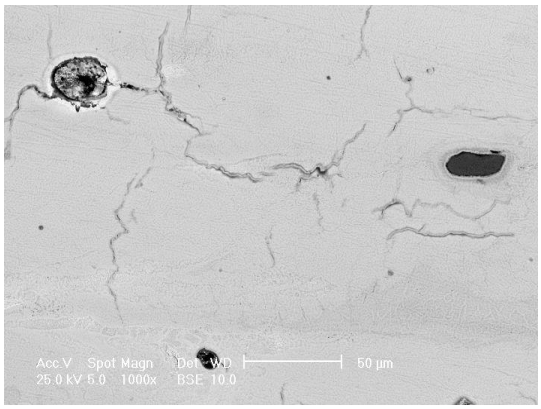

Figure 53 Scanning electron microscopy (1000X) of alloy (3) after solubilisation at 900 °C.

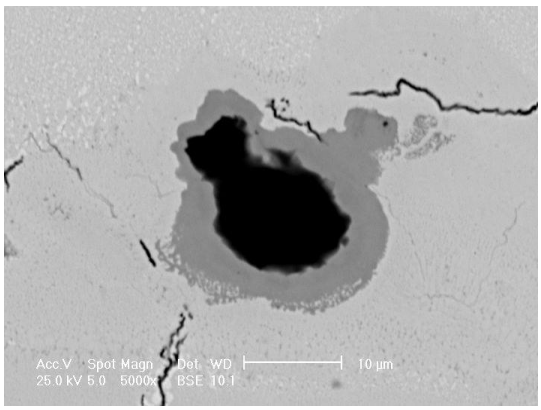

Figure 54 Scanning electron microscopy (500X) of alloy (3) after solubilisation at 900 °C.

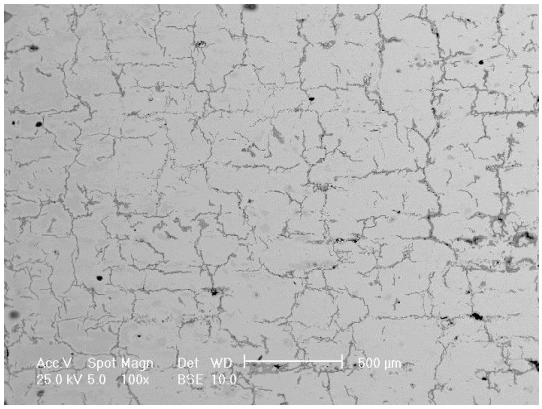

Figure 55 Scanning electron microscopy (100X) of alloy (3) after solubilisation at 1100 °C.

immersed in the precious matrix of yellow colour, similar to what was observed with solid prisms (Figure 43 and 46). As expected, the polished ring made with white gold-titanium alloy is significantly whiter than the ring made with gold-niobium alloy (Figure 60) [10]. Density measurements performed on finished rings have confirmed an expected feature for this alloy, i.e. the low density value. Indeed, values obtained float around 12.0 g $\cdot$ cm^{-3}, i.e. approximately 18% less than a similar sclassical nickel alloy (about 14.6 g $\cdot$ cm^{-3}), and up to 25% less than an equivalent alloy with palladium, the density of which is about 16.0 g $\cdot$ cm^{-3}. The opportunity to have a 18 carat gold alloy (750‰) with a significantly lower density allows to reduce the jewellery weight for a given volume.

Rings underwent an anodizing treatment to verify whether the unique coloring properties of titanium under the action of the electric voltage, could also be transferred to the precious alloy and thus produce a material of innovative appearance. Unfortunately, rings printed using a multiple scan mode (B) and subjected to a classic industrial anodizing process (Figure 61) fail to shown interesting colours. The shade of amber green obtained lacks uniformity, even though the lustre of the polished original piece is partially preserved. The resulting colour may depend in part on the dilution of titanium in the gold matrix, which prevents the formation of the coloured titanium oxide film, but also on other factors correlated to the high applied electric voltage (30-150V), which could lead to gold oxidation, and that certainly require further study.

CONCLUSIONS

Selective laser melting (SLM™) offers numerous potential applications for the manufacture of jewellery items using innovative materials. Amorphous metals can preserve a significant fraction of their glassy phase after the laser printing process, and then continue to offer their amazing mechanical performance, such as high hardness and strength. While the item surface and internal quality still suffer from significant roughness and porosity, results are definitely worthy of consideration given their recent introduction with the selective laser melting technique. Selective laser melting has also demonstrated the possibility to alloy precious matrices with refractory metals, creating thus very hard and white alloys, the manufacture of which would prove nearly impossible with traditional systems. Niobium, for example, has been first incorporated uniformly into a precious gold-zinc matrix by means of selective laser melting; subsequently, the refractory metal has been homogenized through a heat solubilization treatment to produce items featuring hardness and yellow index (D1925) values up to 320 HV and 17.8 respectively. The titanium alloy has been introduced (16.4%p) using a gold-silver matrix in a manner similar to that of niobium, providing exceptional yellow index values (12.60) and nearly equivalent hardness, combined with a greatly reduced density, which is around 25% lower compared to an equivalent alloy with palladium, and 18% lower compared to a conventional white gold-nickel alloy. The complex of residual defects observed in specimens produced is mainly of a microstructural nature and includes microcracks between and transversal to vectors, porosity from partial melting of the metal powder and, secondly, diffuse residue of particles of pure refractory metals not dissolved in the matrix, which can increase the satin-finish of the alloy surface at the expense of its brightness in the finish phase.

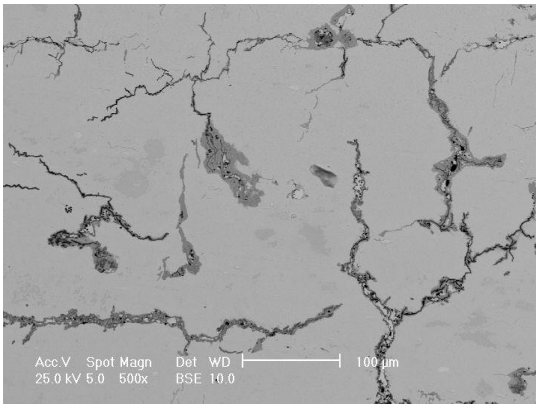

Figure 56 Scanning electron microscopy (500X) of alloy (3) after solubilisation at 1100 °C.

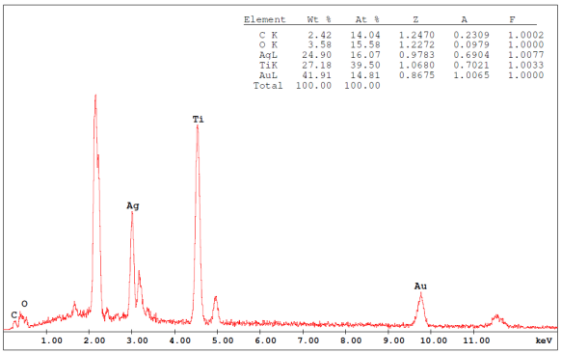

Figure 57 Microanalysis (EDX) of the titanium particle included in the metallic mass (A).

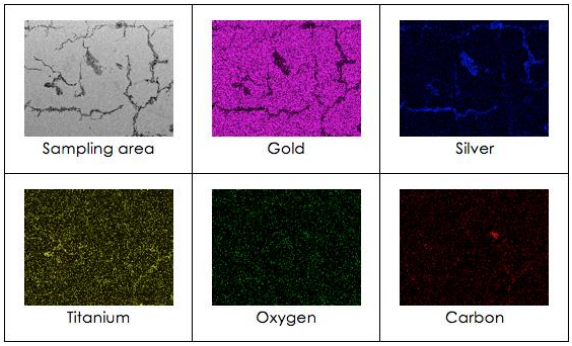

Figure 58 Element map for the alloy (3) after solubilisation at 1100 ° C.

Figure 59 Solid ring (B) printed with alloy (3).

Figure 60 Solid alloy ring (3), newly printed, after polishing.

Figure 61 Ring (B) before and after industrial anodizing.

Progold S.p.A. progold.com +39 (0445) 492600 info@progold.com

BIBLIOGRAPHY

SFS Papers

[1] D. Zito et al., "Latest developments in Selective Laser Melting production of gold jewellery", *The Santa Fe Symposium on Jewelry Manufacturing Technology 2012*, ed. Eddie Bell (Albuquerque: Met-Chem Research, 2012).

[2] D. Zito et al., "Optimisation of the Main Selective Laser Melting Technology Parameters in the Production of Gold Jewellery", *The Santa Fe Symposium on Jewelry Manufacturing Technology 2013*, ed. Eddie Bell (Albuquerque: Met-Chem Research, 2013).

[3] D. Zito et al., "Optimization of SLM Technology Main Parameters in the Production of Gold and Platinum Jewelry", *The Santa Fe Symposium on Jewelry Manufacturing Technology 2014*, ed. Eddie Bell (Albuquerque: Met-Chem Research, 2014).

[4] D. Zito et al., "Definition and solidity of gold and platinum jewels produced using Selective Laser Melting SLM™ technology", *The Santa Fe Symposium on Jewelry Manufacturing Technology 2015*, ed. Eddie Bell (Albuquerque: Met-Chem Research, 2015).

[5] B. Lohwongwatana, J. Schroers, W. L. Johnson, "Liquidmetal – Hard 18K and 850 Pt Alloys That Can Be Processed Like Plastics or Blown Like Glass", *The Santa Fe Symposium on Jewelry Manufacturing Technology 2015*, ed. Eddie Bell (Albuquerque: Met-Chem Research, 2015).

[6] U. E. Klotz, M. Eisenbart, "Gold based bulk metallic glasses - hard like steel, moldable like plastics", *The Santa Fe Symposium on Jewelry Manufacturing Technology 2013*, ed. Eddie Bell (Albuquerque: Met-Chem Research, 2013).

[7] U. E. Klotz, T. Heiss, "Investment Casting of titanium alloys by induction melting", *The Santa Fe Symposium on Jewelry Manufacturing Technology 2015*, ed. Eddie Bell (Albuquerque: Met-Chem Research, 2015).

Article journals
[8] J. Schroers, B. Lohwongwatana, W. L. Johnson, A. Peker, "Gold based bulk metallic glass" *Applied Physics Letters 87*, 061912 (2005).
[9] Hyunbo Shim, Masaki Tahara, Tomonari Inamura, Kenji Goto, Yoko Yamabe-Mitarai, Hideki Hosoda, "Oxidation Behavior of Au-55 mol%Ti High Temperature Shape Memory Alloy during Heating in Ar-50 vol%O_2 Environment" *Materials Transactions*, Vol. 56, No. 4 (2015) pp. 600 to 604.

[10] S. Henderson,D. Manchanda aWhite Gold Alloys: Colour Measurement and Gradingu *Gold Bulletin* 2005, 38/2.